Journal of Applied Polymer Science

Mitigating thermal runaway of lithium-ion battery by using thermally sensitive polymer blend as cathode binder

Anh V. Le,[1] Meng Wang,[1] Daniel J. Noelle,[2] Yang Shi,[2] Yu Qiao [1,2]
[1]Department of Structural Engineering, University of California—San Diego, La Jolla CA 92093-0085
[2]Program of Materials Science and Engineering, University of California - San Diego, La Jolla CA 92093
Correspondence to: Y. Qiao (E-mail: yqiao@ucsd.edu)

ABSTRACT: Thermally sensitive binder (TSB) is developed as an internal safety mechanism of lithium-ion battery (LIB). The TSB is a polymer blend of poly(vinylidene fluoride) (PVDF) and poly(vinylidene fluoride-*co*-hexafluoropropylene) (PVDF-HFP). Compared with regular PVDF binder, the softening and swelling of TSB are more pronounced when temperature is above 110 °C. With the TSB, the cycling performance of LIB cell is not affected; upon nail penetration, the heat generation rate is significantly reduced. The crystallinity of TSB is an important factor. This technology may lead to the development of thermal-runaway-mitigating LIB cells. © 2017 Wiley Periodicals, Inc. J. Appl. Polym. Sci. **2017**, *134*, 45737.

KEYWORDS: applications; batteries and fuel cells; swelling; thermal properties

Received 30 May 2017; accepted 27 August 2017
DOI: 10.1002/app.45737

INTRODUCTION

For the past decade, lithium-ion battery (LIB) has been extensively studied for large-scale energy storage applications, e.g. electric vehicle (EV).[1] To improve the specific energy and energy density, researchers focused on novel architectures of active materials (AMs) as well as electrolyte additives.[2,3] Yet, fire safety and abuse tolerance of LIB have recently gathered increasing concern.[4] For example, if an EV is involved in a traffic accident, internal shorting of LIB cells may occur; local temperature can rapidly increase and the entire battery pack can catch on fire.[5] In a traditional EV battery safety system, the auto frame is designed to deform and absorb impact energy. However, this design imposes constraints on the rigidity and placement of LIB packs and significantly lowers the overall energy and power efficiency.[6] Most importantly, such a system is only effective at the pack level and when the impact loading is mild.[7] In an intense collision, if a single battery cell is heavily deformed, its membrane separator may be torn and uncontrolled discharge would take place directly between the cathode and the anode. As the large amount of electric energy is aggressively dissipated as heat, thermal runaway takes place[8] and local temperature may exceed 300 °C in a fraction of minute, resulting in ignition of the highly flammable electrolyte.[9] It is ideal that thermal-runaway mitigation (TRM) mechanisms can be incorporated into LIB cell components.

Positive temperature coefficient (PTC) material is a widely studied cell-level TRM technique.[5,10] A PTC additive can undergo phase transition at elevated temperature, accompanied by a large increase in electric resistivity. When it is mixed with the AMs in electrode, it can cutoff charge transportation paths in the vicinity of internal short sites before local temperature reaches the onset of thermal runaway. For Lithium Nickel Manganese Cobalt Oxide (NMC) AMs, the onset temperature of thermal runaway is around 170 °C.[11] Other TRM methods include shut-down separators,[11–13] damage homogenizers,[14–16] thermal-runaway retardants,[14,17–19] and deformed current collector.[20]

In a LIB electrode, the particles of AMs are bound together by a polymeric binder, and uniformly spread onto a metal substrate serving as current collector. Very often, poly(vinylidene fluoride) (PVDF) is employed as the binder for cathode, and a mixture of carboxymethyl cellulose and styrene butadiene rubber is the binder for anode.[21] In a recent study, we demonstrated that if the polymer binder was thermally sensitive, it could swell and disintegrate the electrode as the LIB cell reached ~110 °C, which in turn shut down exothermic reactions and suppressed heat generation.[22] The slurry processing with the thermally sensitive binder (TSB) was quite similar to the conventional procedure. TSB was activated at ~110 °C, higher than the upper limit of operating temperature window of LIB cells yet lower than the onset point of thermal runaway. Note that TSB must be compatible with the harsh and high-voltage environment of LIB. Poly(vinylidene fluoride-*co*-hexafluoropropylene) (PVDF-HFP) is an attractive baseline TSB. Kynar Flex

© 2017 Wiley Periodicals, Inc.

Table I. Cathode Binders under Investigation

		Binder components	
	Material code	Component 1	Component 2
Reference binders	B01	PVDF ($M_w \approx 534{,}000$ g mol^{-1})	
	B02	PVDF ($M_w \approx 180{,}000$ g mol^{-1})	
	B03	PVDF-HFP with 32 wt % HFP ($M_w \approx 500{,}000$ g mol^{-1})	
Thermally treated polymer blends	T1-50	B01 (50 wt %)	B03 (50 wt %)
	T1-20	B01 (20 wt %)	B03 (80 wt %)
	T1-10	B01 (10 wt %)	B03 (90 wt %)
	T2-50	B02 (50 wt %)	B03 (50 wt %)
	T2-20	B02 (20 wt %)	B03 (80 wt %)
	T2-10	B02 (10 wt %)	B03 (90 wt %)

2500 is a PVDF-HFP containing 32 wt % HFP; it will be referred to as B03 in this study. The high HFP-content of B03 renders the binder phase more amorphous and prone to swelling in electrolyte.[22] While this characteristic leads to an improved ionic conductivity for electrolyte-hosting membrane separator,[23] when used as a binding material, it results in a relatively poor cycling performance of LIB cell,[22] even with cross-linking treatment and controlled molecular weight.[24] Moreover, the excess electrolyte absorbed by B03 promotes side reactions, forming thick solid-electrolyte interphase (SEI) that worsens the effective conductivity of electrode.

In the current study, we investigate a much-improved TSB: polymer blend of B03 and more stable components, with the crystallinity being optimized. The goal is to suppress heat generation of LIB cell upon nail penetration, and to keep the electrochemical performance unaffected.

EXPERIMENTAL

Sample Processing

Coin Cell Fabrication. For cathode, the AM was $LiNi_{0.5}Mn_{0.3}Co_{0.2}O_2$ (NMC532) (TODA America, product code NCM-04ST). The reference binder was PVDF, with the molecular weight, M_w, of either 534,000 g mol^{-1} (Sigma-Aldrich, product no. 182702) or 180,000 g mol^{-1} (Kynar 711). In the following discussion, they will be referred to as B01 and B02, respectively. Per product specifications from the suppliers, the melting points of B01 and B02 were 171 and 165 °C, respectively. The baseline TSB was B03, as introduced above. Per product specification given by the supplier, the melting point of B03 was in the range 117–125 °C. The conductive additive was carbon black (CB) (TIMCAL C-NERGY Super C65 from TIMCAL). The mass ratio among the dry powders, that is, AM, binder, and CB, was 93:4:3. The positive electrode was processed with 1-methyl-2-pyrrolidone (NMP) (Product No. 328634 from Sigma-Aldrich).

The powder components, that is, AM, binder, and CB, were first dried at 80 °C in a VWR 1410 vacuum oven for 24 h. After drying, they were mixed together in an agate mortar and ground for 45 min. The total mass of the powder mixture was ~5 g. After that, the dry powder mixture was transferred to a 10-mL beaker, to which 2 mL of NMP was added. Slurry mixing was performed with an ultrasonic processor (Qsonica Q55). The processor was set at level 8. The duration of each mixing operation was 1 min, followed by 2 min resting to avoid overheating of the slurry. The mixing-resting process was repeated for 10 times. After that, the wet slurry was cast onto a 15-μm-thick aluminum (Al) foil (MTI Item No. EQ-bcaf-15 u-280), using a film applicator (MTI, EQ-Se-KTQ-100), and the clearance between the blade and the substrate was controlled as 50 μm or 220 μm, for cycle life measurement or nail penetration measurement, respectively. The wet slurries were then transferred to a vacuum oven to remove the NMP solvent. The temperature of the oven was set to 80 °C, and the drying duration was 12 h. After drying, the masses of AM were ~7–8 and 35–40 mg per electrode, respectively, equivalent to 4.4–5 mg/cm^2 and 22–25 mg/cm^2. They were used for cycle life measurement and nail penetration measurement, respectively. The dried cathode films were calendered with a hardened steel double roller, and cut into discs of 14.3 mm diameter.

In an Argon-filled glovebox (Mbraun LABstar MB10/14–150), we assembled and tested cathode half cells in CR2016 stainless steel cases. In each cell, a 14.3-mm-diameter 1.1-mm-thick lithium metal disc was used as the anode. The separator was a 25-μm-thick porous PP/PE/PP trilayer membrane (Product No. 2325 from Celgard), cut into a disc of 15.88 mm diameter. About 10 or 30 μL of electrolyte (BASF SelectiLyte-LP50 EC/EMC) was added into cycle-life-testing cell or nail-penetration-testing cell, respectively. Neither spacer nor spring was added in the cathode half cell.

Treatment of TSB. Table I lists the cathode binders investigated in our experiments. The reference binders were B01, B02, and B03. The former two were PVDF with different molecular weights, commonly employed as binders in regular LIB electrodes; B03 was an amorphous PVDF-HFP, prone to swelling in electrolyte at elevated temperature. The volumetric stability of B03 was quite poor in electrolyte under normal working condition of LIB, during the repeated lithiation and de-lithiation process. To keep the high thermal sensitivity and also improve the room-temperature stability of the binder, we blended B03 with PVDF (B01 or B02), and also performed thermal treatment.

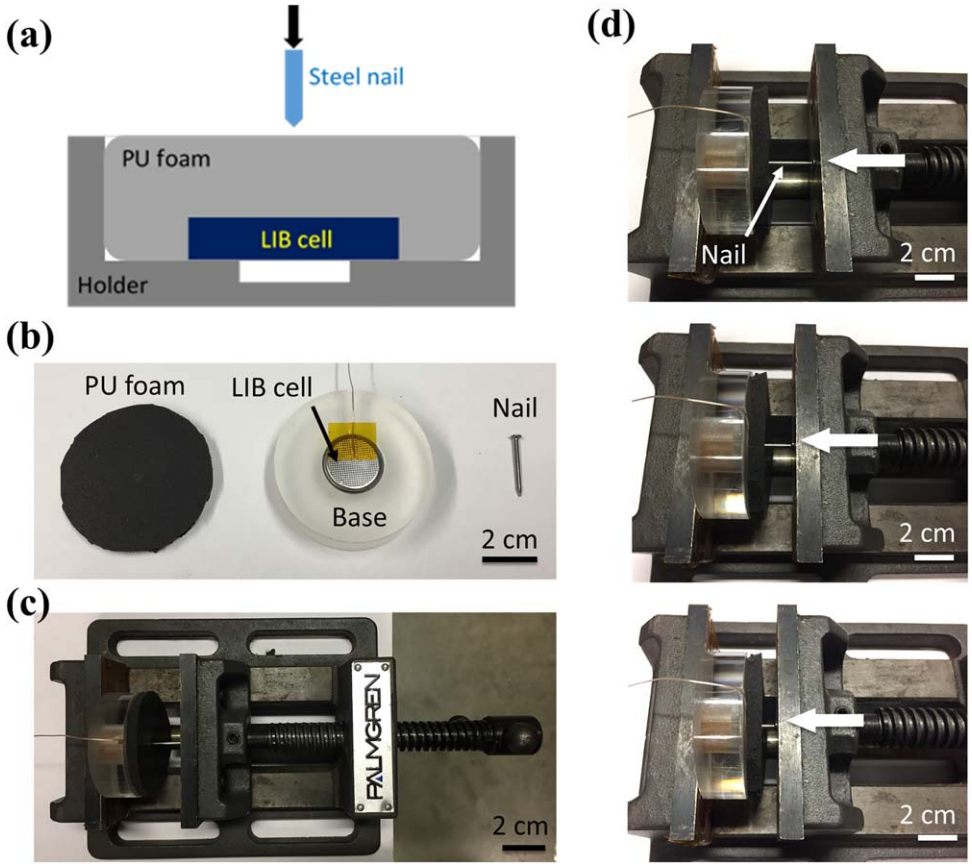

Figure 1. (a) Schematic of the experimental setup of nail penetration. (b) A typical sample assembly. (c) Photo of a testing sample mounted in bench vice. (d) Photos of testing sample before (top), during (middle), and after (bottom) nail penetration. [Color figure can be viewed at wileyonlinelibrary.com]

Before binder processing, all dry powders were dried in a vacuum oven at 80 °C for 24 h. After drying, either B01 or B02 was added to B03 with the ratio specified in Table I. The polymer mixture was then added together with AM and CB with the mass ratio of AM:binder:CB = 93:4:3. The powder mixture was manually ground in an agate mortar for 45 min, and transferred to a 10-mL beaker for slurry processing, following a similar procedure as described above.

Thermal treatment was performed on dried electrode films, before calendering. The electrode films were heated to 200 °C, above the melting point of the binder components, in a Carbolite CTF 12 furnace with no purge gas. The heating rate was 10 °C min^{-1}. The furnace temperature was maintained at 200 °C for 1 h, and then slowly cooled down to room temperature. The cooling rate was about 20 °C h^{-1}. When the temperature, *T*, was ~20 °C below the melting point of each binder component (140 °C for B01, 140 °C for B02, and 80 °C for B03), the temperature was maintained constant for 1 extra hour to promote crystallization, followed by continued cooling. After the thermal treatment, the electrode films were calendered, cut into small discs, and assembled into coin cells, following the same procedure described above.

Coin Cell Testing

For cycle life testing, the cells were charged-discharged between 4.3 and 3.0 V at 60 °C, using a MTI BST8-3 Battery Analyzer. The elevated temperature was maintained by a heating chamber. The chamber was connected to a Digitrol II temperature controller (Product No. Z285498 from Sigma-Aldrich). To promote uniform SEI formation, the first cycle was carried out at C/10 rate, with an applied current of 148 mA/g. The following cycles were performed at 1C. The data were taken from the 11th cycle.

Nail penetration test was performed to investigate the heat generation in a battery undergoing severe internal shorting. The cells were pre-cycled, fully charged, and pre-heated prior to the nail penetration test. Pre-cycling and charging of battery cells were performed with the MTI BST8-3 Battery Analyzer at ambient temperature. First, the cells were charged and discharged between 4.3 and 3.0 V at C/10 rate for 1 cycle, to facilitate uniform SEI formation. Then, the cells were cycled between 4.2 and 3.0 V at C/2 rate for five cycles, and finally charged to 4.6 V at C/10 rate. The relatively high final voltage led to a high specific energy of testing sample. The final capacity of each cell was ~5 mAh, equivalent to ~3.1 mAh/cm^2. At the fully charged state, the cells were preheated on a hot plate (Corning PC 4000) at 110 °C for 1 min. After preheating, the cells were cooled in air for 10 min, to reach room temperature (~23 °C), with the final voltage stabilized around 4.50–4.52 V.

The setup of nail penetration measurement was previously developed in Ref. 15 (Figure 1). The battery cell was placed at

the center of a polyurethane (PU) container, secured by insulating tapes. An Omega TT-K-40–25 type-K gage-40 thermocouple was attached to the cell case to measure the temperature. The tip of the thermocouple was placed ~2.5 mm away from the center of the cell, secured by Kapton tapes. The thermocouple was connected to a temperature logger (Omega OM-EL-USB-TC) for data recording. A 1-cm-thick layer of PU foam was placed on top of the cell for thermal insulation. A stainless steel nail with the diameter of 1.58 mm was used to trigger internal shorting. The nail was driven through the center of the battery cell using a Palmgren bench vise.

Material Characterization

Environmental Scanning Electron Microscopy. After the nail penetration test, the electrodes were taken out from the cell case in the glovebox, attached to an environmental scanning electron microscopy (ESEM) sample stage, and sealed in a polyethylene vacuum bag. Then, they were quickly transferred to the ESEM chamber. ESEM analysis was performed in vacuum to study the microstructure of electrode at different stages: (i) immediately after pre-cycling and charging, (ii) immediately after preheating, and (iii) after nail penetration. The electrodes were taken out of the cell case as-is and cut into small pieces.

Differential Scanning Calorimetry. Differential scanning calorimetry (DSC) analyses were performed on bulk polymers to investigate their melting behaviors in both absence and presence of electrolyte. A total of 2 g of polymer powders were dissolved in 5 mL NMP, forming a gel. The gel was cast as a 1-mm-thick coating onto a flat glass plate. Solution mixing and casting were performed by using the same ultrasonic processor and doctor blade as in "Sample Processing section". The gel was dried in a vacuum oven at 80 °C for 24 h. A 6.35-mm-diameter disc was cut from the dried polymer film, weighing ~10 mg and about 200 μm thick.

Two groups of polymer films were investigated: dry polymer discs (Group 1) and polymer discs soaked up with electrolyte for 3 h (Group 2). Soaking was performed in the Argon-filled glovebox. After soaking, the sample mass increased by ~2 mg. The sample was placed in a 50 μL sealed aluminum (Al) pan.

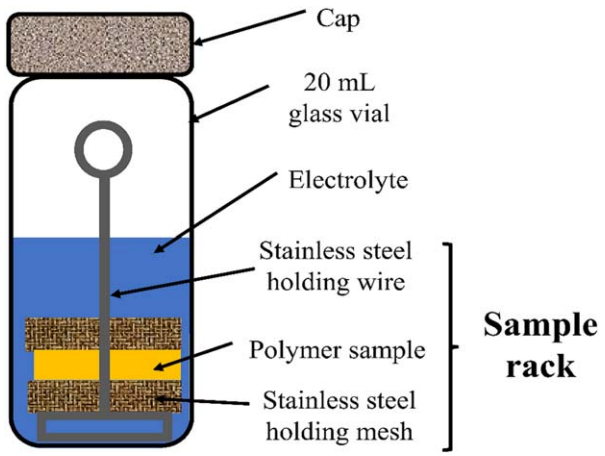

Figure 2. A testing sample for the swelling index (SI) measurement. [Color figure can be viewed at wileyonlinelibrary.com]

DSC analyses were performed in a DSC 8000 (PerkinElmer) machine. For each run, the reference was an empty sealed pan, that is, with no polymer sample but only Argon gas. The sample was heated from 40 to 200 °C at the rate of 10 °C min^{-1}.

Swelling Index Measurement. To determine the degree of dissolution and the degree of swelling of each type of binder material in electrolyte, we performed swelling index (SI) measurement. The experiment followed ASTM D3616-95 (2014), with the procedure being simplified to accommodate the small sample size (Figure 2). Polymer films were prepared through a similar procedure as described in "Environmental Scanning Electron Microscopy section", except that the gel coating thickness was about 400 μm. After drying in a vacuum oven for 24 h, the final film thickness was ~100 μm. The dried polymer film was cut into "rings" of 12.7 mm outer diameter and 3.2 mm inner diameter. The initial mass of each "ring" was ~20 mg. Each sample consisted of 5 "rings," with the total mass (m_i) ~100 mg per sample.

The sample was sandwiched between two 12.7-mm-diameter stainless-steel meshes. Reference test was carried out without polymer, that is, $m_i = 0$. The sample rack was submerged in 10 mL of electrolyte, with initial mass of M_{EL}. The experimental apparatus was assembled in the Argon-filled glovebox and sealed with parafilm (Pechiney PM 996) before being transferred out for testing. The SI tests were carried out at three different temperatures: 25, 60, and 80 °C. The testing duration was 24 h.

After 24 h, the unit was opened, and 2.5 mL of liquid, containing electrolyte solvent and polymer solute, was pipetted out onto an Al weighing dish and vacuum dried for 24 h. The mass of the dried gel was measured and recorded as m_g. The mass of dissolved polymer was calculated as:

$$m'_d = 4 \times m_g \quad (1)$$

In eq. (1), the factor of 4 accounted for that only 25% of electrolyte was sampled for the measurement of m_g. To account for the residual electrolyte present in the dried gel, we performed a calibration test in which the electrolyte was vacuum-dried at 80 °C for 24 h, and measured a constant amount of $r = 7.62$ wt % solid left.

Let m_d be the actual mass of dissolved polymer and m_s be the mass of solid component of the electrolyte in the electrolyte/polymer solution. Then,

$$m'_d = m_d + m_s, \quad (2)$$

and the actual mass of the electrolyte solvent in the electrolyte/polymer solution was:

$$m'_{EL} = m_s / r \quad (3)$$

The mass of the undissolved polymer was:

$$m_p = m_i - m_d = m_i - m'_d + m_s \quad (4)$$

To calculate the SI, the solvent must be completely removed. This was done by gently washing the sample with fresh solvent, that is, the electrolyte. The washing solvent was removed, and the masses of the sample containing rack and the reference empty rack were quickly measured and recorded as m_r and $m_{r,\mathrm{ref}}$, respectively. Then, the mass of the swollen polymer

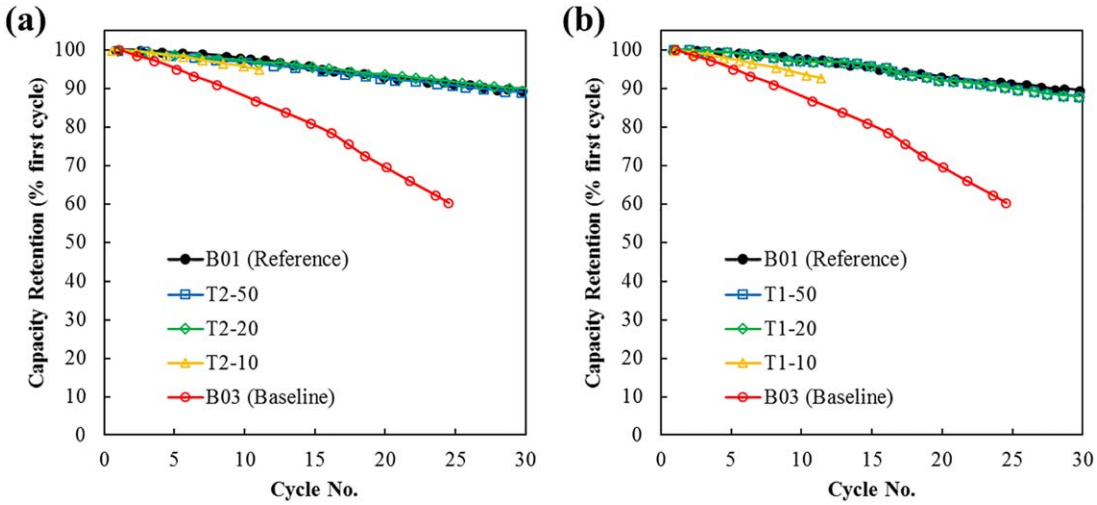

Figure 3. Typical cycling performance of LIB cathode half-cells based on: (a) thermally treated B01/B03 blends and (b) thermally treated B02/B03 blends. The legend indicates the binder codes. The testing temperature is 60 °C. [Color figure can be viewed at wileyonlinelibrary.com]

sample, containing both the undissolved polymer and the solvent that entered the polymer system, was given by:

$$m_{sw} = m_r - m_{r,\mathrm{ref}} \tag{5}$$

The mass of the electrolyte in the swollen polymer was:

$$m_{EL} = m_{sw} - m_p = m_{sw} - m_i + m_d - m_s \tag{6}$$

Because the initial mass of electrolyte in the system M_{EL} was known, and $M_{EL} = m_{EL} + m_{EL}'$, we could solve for m_s from eqs. (3) and (6) and the actual mass of polymer in the dried gel, m_d, could be calculated. The weight percentage of dissolved polymer was given by:

$$D(\%) = (m_d/m_i)\times 100 \tag{7}$$

Finally, the SI was calculated as the ratio between the mass of swollen (electrolyte containing) polymer, m_{sw}, and the mass of the undissolved polymer component, m_p:

$$\mathrm{SI} = m_{sw}/m_p \tag{8}$$

RESULTS AND DISCUSSION

The goal of increasing the temperature of cycling test of LIB cells is to accelerate the aging of electrode while maintain it within the safe operation temperature window.[26] As shown in Figure 3, the electrochemical performances of polymer-blend-based LIB cells are comparable with or slightly better than that of B01-based reference cell, by far exceeding the performance of B03-based cell. In general, as the PVDF content in polymer blend increases, the cycling performance is improved. When the PVDF component is B01, as the binder changes from T1–10 to T1–20, the degradation rate is reduced by nearly 40%; as the binder changes to T1–50, the degradation rate is further decreased by another ~20%, lower than yet close to that of B01-based reference cell. When the PVDF component is B02, while the curves of T2–10-based and T1–20-based cells are somewhat similar, as the PVDF content in binder rises to 20%, T2–20-based cell demonstrated the best performance, superior to the reference cell. However, as the B02 content in polymer blend increases to 50%, the degradation rate of T2–50-based cell slightly increases to above that of B01-based reference cell, suggesting that the beneficial effects of blending B03 with PVDF has saturated.

The purpose of blending B03 with either B01 or B02 is to reduce the amount of unstable PVDF-HFP in the binder phase. The thermal treatment is conducted to promote the formation of crystalline phases of both PVDF and PVDF-HFP, so that the structural properties are enhanced.[25] In general, slow cooling promotes crystallization of polymer. It has been reported that annealing of PVDF helped maximize the crystalinity.[25] Both B01 and B02 are PVDF, proven stable and durable in the electrochemical environment of LIB cell. They possess different molecular weights and structures. As the polymer blend is cooled down, B01 or B02 solidifies first, since their melting points are much higher than that of B03. As temperature further decreases, B03 molecules attach onto PVDF nuclei and NMC532 microparticles. The PVDF nuclei may increase the crystallinity of the PVDF-HFP, as it is more energetically favorable for the B03 chains to align with the crystalline B01 or B02 phase. The high cycling performance of the B02-containing cells is attributed to the higher crystallinity of B02, which is confirmed by our DSC analysis results.

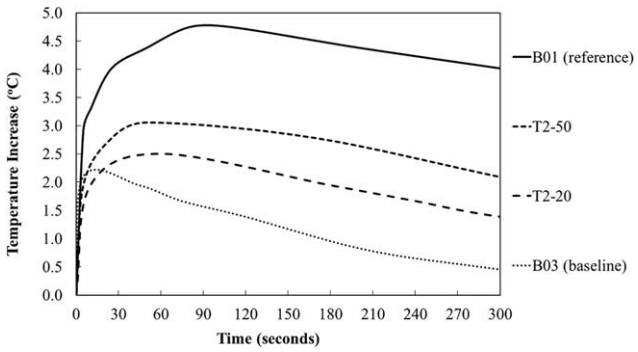

Figure 4. Typical temperature profiles measured in nail penetration tests. The legend indicates the binder codes.

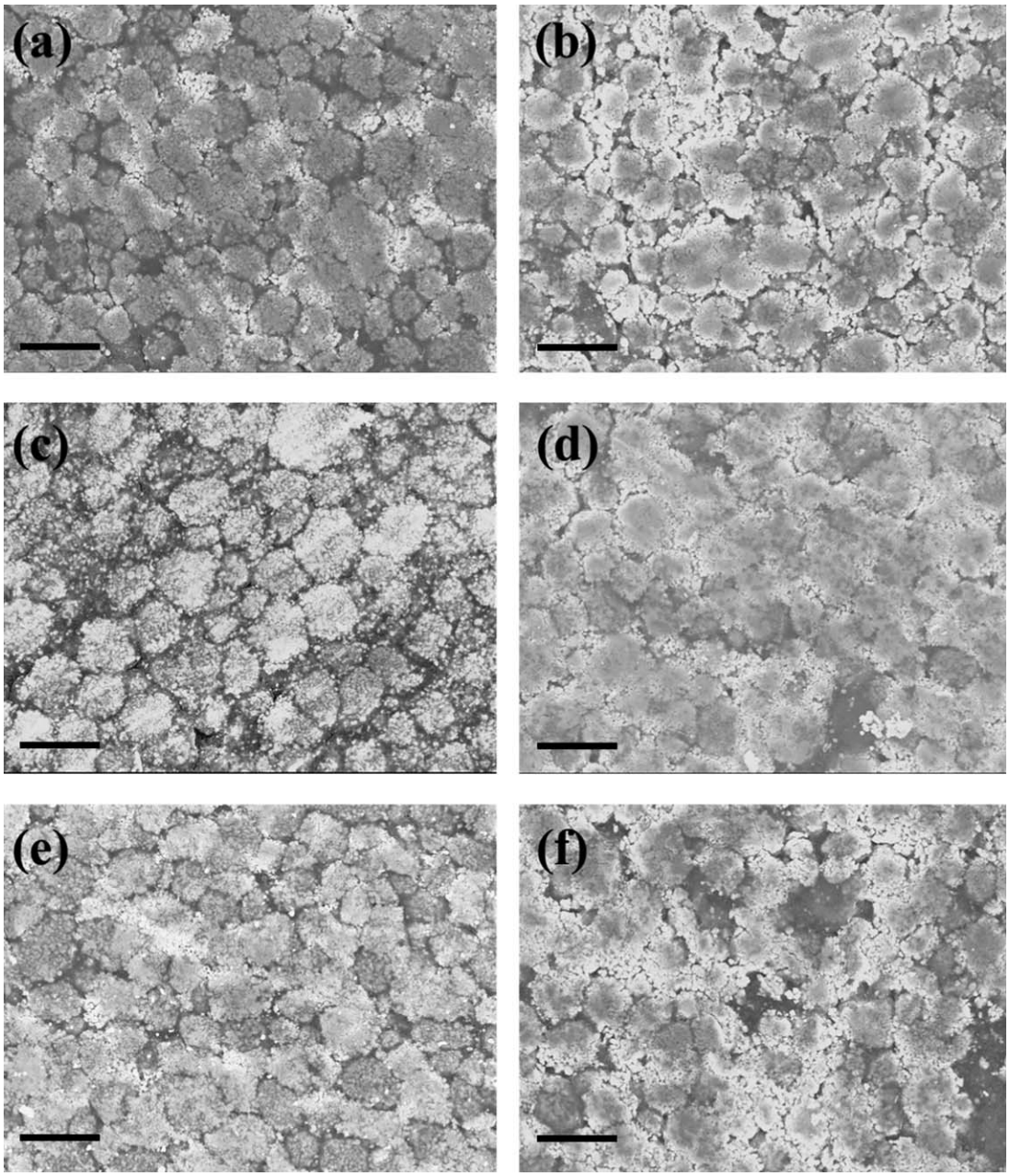

Figure 5. SEM images of reference positive electrodes (a,c,e) and T2–20-based positive electrodes (b,d,f) at different stages: after cycling and charging (a,b), after preheating at 110 °C (c,d), and after nail penetration (more than 0.5 cm away from the nail) (e,f). The scale bars indicate 20 μm.

PVDF possesses a higher crystallinity and is more stable than PVDF-HFP, which offers a better structural support to the electrode. However, if the crystallinity of polymer binder is too high, it might not store enough electrolyte to maintain a sufficient ionic conductivity. Because B02 and B03 are immiscible, as will be shown by the DSC results, the nonuniformly distributed B02 crystalline regions may cause heterogeneity in lithiation and delithiation, leading to stress concentration that hampers the long-term performance of electrode. In other words, while a high concentration of B02 in binder blend may increase the structural integrity and solvent resistance, it may also impose a negative effect on the ionic conductivity and introduce more internal stresses during cell cycling. Therefore, the composition of polymer blend must be optimized. According to our testing result, the optimum PVDF content is around 20%.

For small LIB CR2016 coin cell, nail penetration is a reliable method to establish internal short circuit.[27] Joule heating "plays a key role in initiating the temperature rise at the point of short".[28] In this study, the amount of energy stored in each coin cell is limited, so that the shorted cell cannot reach 170 °C, where thermal runaway takes off with aggressive exothermic reactions. Therefore, Joule heating is the only source of heat generation. Nevertheless, the amount of heat generated can be evaluated via the peak temperature increase of the cell (ΔT_{peak}). The nail penetration testing results (Figure 4) confirm that the T2–20-based cell shows significant reduction in ΔT_{peak}

compared to the reference B01-based cell. Compared with B03-based cell, ΔT_{peak} of T2–20-based cell is higher by only ~10%; the post-peak temperature decrease rate is substantially higher, but it is not the critical element for TRM. That is, T2–20-based cell generates more heat than B03-based cell within the first 5 min, yet the heat generation is distributed over a relatively long time and thus, does not have a significant effect on the maximum temperature increase. Peak temperature increase is the critical parameter to evaluate Joule heating in a shorted coin cell. In a long run, the normalized total released heat (kJ Ah^{-1}) should be similar for all the cells, as it is determined by the total stored energy. The peak temperature increase for the reference cell with B01 binder is ~4.75 °C. The peak temperature increase for a T2–20-based cell is ~2.5 °C.

The working mechanism of T2–20 should be similar to that of B03. That is, at the preheating temperature of 110 °C, the crystalline portion of B03 melts and creates more amorphous regions, resulting in a significant and sudden volume increase associated with swelling as well as a considerable reduction in free electrolyte. Binder swelling loosens the contact between the conductive binder-CB network and the AM microparticles, which increases the electrical conductivity of the electrode, limiting the discharge current rate and thus, reducing the Joule heating rate. The rate at which the heat is generated is lowered while the rate at which it diffuses into the surrounding environment remains almost the same. Therefore, the amount of heat built up in the system is limited, so is the peak temperature increase. In the actual energy storage system of an EV, the capacity of each battery cell is about three orders of magnitude larger and may easily reach 170 °C in less than a minute.[28] If the peak temperature increase in these higher-capacity cells can be reduced by ~40%, the risk of thermal runaway may be significantly lowered.[29,30] Note that the relationship between cell size and ΔT_{peak} is nonlinear and is also dependent on other factors such as battery chemistry, state of charge, geometry, and ambient temperature.[31] Therefore, the effectiveness of TSB must be re-evaluated for different LIB systems. Regardless, the nail test results clearly demonstrate the potential of TRM by using TSB. In the current TSB design, the swelling of PVDF-HFP amorphous phase during normal charge-discharge operation is restricted by PVDF.

Figure 5 shows the reference and the T2–20-based cathodes at different stages. After pre-cycling and charging, both electrodes exhibit good uniformity [Figure 5(a,b)], which explain the similar cycling performances of B01 and T2–20 cells [Figure 3(b)]. Note that T2–20 is distributed more uniformly around AM particles, probably because that the B03 component of binder interacts with NMP more completely during slurry processing. In addition, B03 is also more flexible and deformable, while B01 is stiffer and has a higher resistance to calendering.

After preheating, the B01-based electrode remains densely packed [Figure 5(c)], while considerable swelling of binder can be observed in T2–20-based electrode: the binder-filled regions among AM particles are up to 10 μm in size [Figure 5(d)]. However, these regions are sparsely dispersed, which may be attributed to the immiscibility of the B02 phase and the B03 phase in the T2–20 blend (Figure 6). In the swollen binder, both bonding strength and electrical conductivity are reduced. Due to the sparse distribution of weakened regions, the T2–20-based electrode is still relatively structurally stable under short discharge. After nail penetration, the T2–20-based electrode shows almost no prominent cracks [Figure 5(f)]. The enlarged binder-filled regions may be related to the effect of nail loading on the weakened regions. The reduction in temperature increase of T2–20-based cell (Figure 4) should be largely associated with the increase in electrical resistivity.

Figure 6 shows the DSC measurement results of PVDF binders and PVDF/PVDF-HFP blends. The crystallinity can be assessed from the heat of fusion, ΔH_f. The higher the value of ΔH_f, the higher the crystallinity.[32] The values of ΔH_f are given in Table II. Both dry [Figure 6(a)] and electrolyte-soaked [Figure 6(b)] B03 films show broad shoulders, which can be attributed to the wide distribution of molecular weight.[32] Melting of dry B03 begins at about 80 °C. In the presence of electrolyte, the melting temperature range is reduced by about 15–20 °C, and the heat absorption is also much reduced. As a result, the electrolyte-soaked B03 film starts to relax around 50 °C. Such a low-temperature relaxation explains the poor cycling performances of LIB cells based on pristine B03.[21] Pristine B03 offers relatively low strength, low solvent resistance, and low thermal stability. In comparison, both pristine PVDF reference materials, that is, B01 and B02, possess higher crystallinity than B03. The computed values of ΔH_f show that B02 has a higher degree of crystallization than B01 (Table II), probably because that the shorter chains of B02 are less entangled. Note that crystallinity is not the only indicator for the strength of polymer. High entanglement density of longer chains also enhances the strength. However, when the PVDF binder is attacked by a solvent, the amorphous regions swell, so that the crystalline

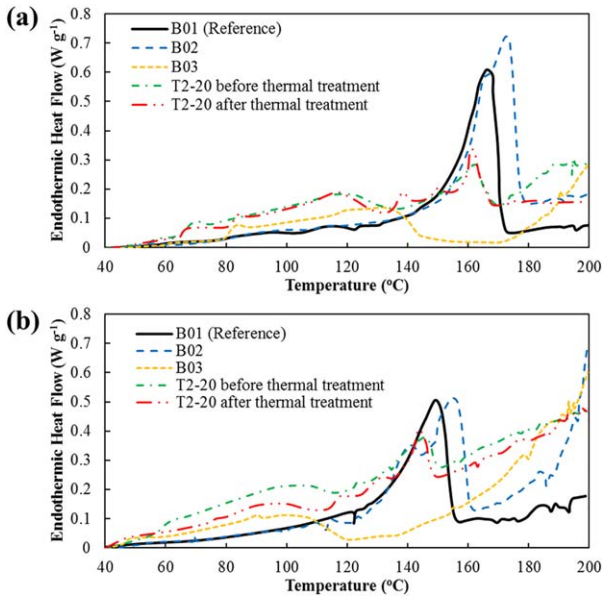

Figure 6. Typical DSC curves of various cathode binders: (a) dry polymer films (Group 1) and (b) polymer films soaked in electrolyte (Group 2). [Color figure can be viewed at wileyonlinelibrary.com]

Table II. Average Heat of Fusion of Cathode Binder, ΔH_f (J g^{-1})

Material code		Group 1: Dry polymer films	Group 2: Polymer films soaked in electrolyte
B01		44.1	29.4
B02		40.3	38.6
B03		20.7	13.8
T2-20, before thermal treatment	B02 phase	35.7	30.6
	B03 phase	18.6	10.8
T2-20, after thermal treatment	B02 phase	61.8	48.6
	B03 phase	19.9	10.0

regions play the major role in supporting the polymer matrix. Therefore, B02-containing cells show a better cycling performance than B01-containing cells (Figure 3).

Regardless of the thermal treatment and presence of electrolyte, all B02/B03 blends exhibit two separate endothermic melting peaks, associated with melting of B03 and B02, respectively (Figure 6). It indicates that the two components in the blend, that is, B03 and B02, are immiscible to each other.[33] In fact, immiscibility is preferred to preserve the thermal instability of B03, which is needed for TRM, and to maintain the high strength of B02 under normal working condition. The independent melting behaviors of B02 and B03 phases render the assessment of their crystallinity relatively easy. While the heat of fusion of neat polymer can be directly computed through DSC analysis, the true value of ΔH_f of each component in polymer blend can be different. The content of electrolyte in soaked samples has also been subtracted before DSC scanning. For instance, a T2–20 sample contains 20 wt % of B02 phase, and the DSC scan of this sample gives a raw value of 9.72 J g^{-1} for ΔH_f of B02. The adjusted ΔH_f value of B02 is (9.72 J g^{-1})/(20%) = 48.6 J g^{-1}.

With thermal treatment, the crystallinity of B02 in T2–20 increases by 73% in dry polymer film, and by 59% in polymer film soaked with electrolyte, as shown in Table II. The increase in crystallinity of B02 is mostly associated with the formation of relatively small-sized crystalline areas, reflected by the smaller melting peaks in the DSC curves within the 132–155 °C range for dry T2–20 [Figure 6(a)] and within the 115–135 °C range for soaked T2–20 [Figure 6(b)]. As shown in Figure 6(b), after heat treatment, the melting peak of B03 phase is reduced by ~20 °C, shifted to below 110 °C; therefore, the thermal sensitivity of binder is enhanced. The effect of heat treatment can also be seen in Table II. The heat of fusion of the B02 phase in electrolyte increases from 30.6 to 48.6 J/g, indicating an increased stability of B02 phase at elevated temperature. The DSC curves also support our hypothesis that the PVDF phase offers nucleation sites for the crystallization of PVDF-HFP: Smaller crystalline areas of B03 are indicated by the smaller melting peaks in the DSC curve of dry T2–20 within the 65–88 °C range. Interestingly, the crystallinity of B03 phase remains relatively constant (Table II). The melting peak of smaller B03 crystalline regions vanishes when the polymer blend is soaked in electrolyte, possibly due to the solvent attack. The solvent attack is also evident in PVDF, but much less severe: The heights of smaller melting peaks of B02 are reduced, yet the shapes of these peaks are prominent. Regardless, the 59% increase in crystallinity of B02 phase in electrolyte-soaked T2–20 enhances the structural integrity of electrode [Figure 3(b)].

After thermal treatment, the major melting peaks of B03 in T2–20, both in dry and electrolyte-soaked samples, slightly shift to the left, suggesting that melting of semi-crystalline B03 occurs at a slightly lower temperature. For polymer in dry state, melting still completes well over 110 °C; the benefit becomes evident for the polymer films soaked in electrolyte, as the melting peaks are reduced by ~20 °C. As a result, the entire melting curve of B03 in thermally treated T2–20 shifts to below 110 °C (Figure 4).

SI measurement provides additional information about the working mechanism of TSB (Table III). Overall, the dissolution and swelling of all the polymers in the current investigation are quite pronounced. The final dried polymer gel exhibits a substantial mass loss (m_d). The polymer samples of SI measurement are processed without any AM or CB. That is, there are

Table III. Swelling Indices (SI) of Cathode Binders

	At room temperature		At 60 °C		At 80 °C		
Polymer binder	% Dissolved	SI	% Dissolved	SI	% Dissolved	SI	Lower limit of melting point, $T_{m,\ onset}$ (°C)
B01	28.31	6.55	23.90	5.37	17.41	5.83	~140
B02	21.77	4.82	23.20	4.89	20.73	5.99	~147
B03	34.22	7.95	61.80	11.90	100.00	—	~85
					—	21.42	
T2-20	26.60	5.94	49.06	6.63	58.00	9.65	

fewer nucleation sites and reinforcement against dissolution and swelling.[34,35] In addition, the excess amount of electrolyte may promote swelling and dissolution. Hence, the measurement results are valid only for self-comparison among the bulk polymers.

At room temperature, the PVDF materials, B01 and B02, show mild dissolution and swelling, while the high-HFP-content copolymer, B03, shows more pronounced dissolution and swelling, since it contains more amorphous phase. When B03 is blended with B02 at the optimized ratio and after the thermal treatment, dissolution and swelling of T2–20 at room temperature can be much reduced to the same level as B01 and B02, and thus, helps stabilize the cycling performance of T2–20-based LIB cells [Figure 3(b)].

As the temperature increases to 60 and 80 °C, dissolution and swelling of B03 become more and more severe, while B01 and B02 remain mostly unaffected. At 80 °C, bulk B03 is completely dissolved in electrolyte. At 60 °C, the SI of B03 increases by ~50% and is more than two times higher than the swelling indices of B01 and B02. The SI of T2–20, however, increases by only 12%, and only about 23% higher than that of the reference B01 binder. The improved swelling resistance can be attributed to the presence of B02 in the system, aided by the thermal treatment that increases the crystallinity. Note that the swelling indices of B02 at room temperature and at 60 °C are both lower than those of B01 at the same temperatures, respectively, which agrees with the DSC results that the crystallinity of B02 is higher (Table II). The dissolution level of T2–20 at 60 °C, while improved from the pristine B03, is still about twice of those of PVDF materials. It suggests that if the content of T2–20 in the electrode is reduced by about 50%, binder dissolution and swelling may be further reduced, beneficial to long term cycling performance.

CONCLUSIONS

Thermally sensitive binder (TSB) of lithium-ion battery (LIB) cathode half-cells are investigated. The TSB are based on a PVDF-HFP copolymer with 32 wt % HFP content, blended with a PVDF homopolymer, with the crystallinity being enhanced by thermal treatment. The capacity retention of TSB-based LIB cell can be better than that of PVDF-based reference cell, and the peak temperature increase in coin cell subjected to nail penetration is reduced by ~50%. The superior performance of the polymer blend binder can be attributed to the stabilization effect of the crystalline PVDF phase within the operating temperature window of LIB cell, and the melting and swelling of the electrolyte-containing PVDF-HFP phase at elevated temperature. The optimum PVDF content is TSB is around 20%. This finding may lead to the development of thermal-runaway-mitigation techniques of LIB cells. Future research on full-size pouch cells and higher-energy active materials should be performed to further validate the concept of TSB.

ACKNOWLEDGMENTS

This research is supported by the Advanced Research Projects Agency–Energy (ARPA-E) under Grant No. DE-AR0000396, for which we are grateful to Dr. Ping Liu, Dr. John Lemmon, Dr. Grigorii Soloveichik, Dr. Chris Atkinson, and Dr. Dawson Cagle. Special thanks are also due to Drs. Jiang Fan and Dengguo Wu for the help with the LIB design and processing.

REFERENCES

1. Lu, L.; Han, X.; Li, J.; Hua, J.; Ouyang, M. *J. Power Sources* **2013**, *226*, 272.
2. Sun, Y. K.; Chen, Z.; Noh, H. J.; Lee, D. J.; Jung, H. G.; Ren, Y.; Wang, S.; Yoon, C. S.; Myung, S. T.; Amine, K. *Nat. Mater.* **2012**, *11*, 942.
3. Abele, A.; Elkind, E.; Intrator, J.; Washom, B. 2020 Strategic Analysis of Energy Storage in California. University of California, Berkeley School of Law **2011**.
4. Roth, E. P.; Orendorff, C. J. *Interface* **2012**, *21*, 45.
5. Doughty, D. H.; Roth, E. P. *Soc. Interface* **2012**, *21*, 37.
6. Arora, S.; Shen, W.; Kapoor, A. *Renew. Sustain. Energy Rev.* **2016**, *60*, 1319.
7. Xia, Y.; Wierzbicki, T.; Sahraei, E.; Zhang, X. *J. Power Sources* **2014**, *267*, 78.
8. Finegan, D. P.; Scheel, M.; Robinson, J. B.; Tjaden, B.; Hunt, I.; Mason, T. J.; Millichamp, J.; Di Michiel, M.; Offer, G. J.; Hinds, G.; Brett, D. J. *Nat. Commun.* **2015**, *6*,
9. Feng, X.; Sun, J.; Ouyang, M.; Wang, F.; He, X.; Lu, L.; Peng, H. *J. Power Sources* **2015**, *275*, 261.
10. Balakrishnan, P. G.; Ramesh, R.; Kumar, T. P. *J. Power Sources* **2006**, *155*, 401.
11. Golubkov, A. W.; Fuchs, D.; Wagner, J.; Wiltsche, H.; Stangl, C.; Fauler, G.; Voitic, G.; Thaler, A.; Hacker, V. *RSC Adv.* **2014**, *4*, 3633.
12. Ozawa, K. *Solid State Ionics* **1994**, *69*, 212.
13. Laman, F. C.; Gee, M. A.; Denovan, J. *J. Electrochem. Soc.* **1993**, *140*, L51.
14. Qiao, Y.; Lu, W.; Shi, Y.; Le, A. U.S. Pat. **2016**, 535.
15. Le, A. V.; Wang, M.; Shi, Y.; Noelle, D. J.; Qiao, Y.; Lu, W. *J. Appl. Phys.* **2015**, *118*, 085312.
16. Le, A. V.; Wang, M.; Shi, Y.; Noelle, D. J.; Qiao, Y. *J. Phys. D: Appl. Phys.* **2015**, *48*, 385501.
17. Wang, M.; Le, A. V.; Shi, Y.; Noelle, D. J.; Yoon, H.; Zhang, M.; Meng, Y. S.; Qiao, Y. *J. Mater Sci. Technol.* **2016**, *32*, 1117.
18. Shi, Y.; Noelle, D. J.; Wang, M.; Le, A. V.; Yoon, H.; Zhang, M.; Meng, Y. S.; Qiao, Y. *ACS Appl. Mater. Interfaces* **2016**, *8*, 30956.
19. Shi, Y.; Noelle, D. J.; Wang, M.; Le, A. V.; Yoon, H.; Zhang, M.; Meng, Y. S.; Qiao, Y. *J. Power Sources* **2016**, *326*, 514.
20. Wang, M.; Le, A. V.; Shi, Y.; Noelle, D. J.; Yoon, H.; Zhang, M.; Meng, Y. S.; Qiao, Y. *Int. J. Damage Mech.* **2016**, 1056789516660176.
21. Chou, S. L.; Pan, Y.; Wang, J. Z.; Liu, H. K.; Dou, S. X. *Phys. Chem. Chem. Phys.* **2014**, *16*, 20347.
22. Le, A. V.; Wang, M.; Noelle, D. J.; Shi, Y.; Yoon, H.; Meng, Y. S.; Wu, D.; Fan, J.; Qiao, Y. *Int. J. Energy Res.* **2017**. in press

23. Song, M. K.; Kim, Y. T.; Kim, Y. T.; Cho, B. W.; Popov, B. N.; Rhee, H. W. *J. Electrochem. Soc.* **2003**, *150*, A439. 2003
24. Le, A. V.; Wang, M.; Noelle, D. J.; Shi, Y.; Yoon, H.; Zhang, M.; Meng, Y. S.; Qiao, Y. *J. Appl. Polym. Sci.* **2017**, *134*, DOI: 10.1002/app.45078.
25. Nakagawa, K.; Ishida, Y. *J. Polym. Sci. Polym. Phys.* **1973**, *11*, 2153.
26. Waldmann, T.; Wilka, M.; Kasper, M.; Fleischhammer, M.; Wohlfahrt-Mehrens, M. *J. Power Sources* **2014**, *262*, 129.
27. Kim, G.-H.; Smith, K; Pesaran, A. Lithium-Ion Battery Safety Study Using Multi-Physics Internal Short-Circuit Model. The 5th Intl. Symposium on Large Lithium-Ion Battery Technology and Application; Long Beach, CA; **2009**.
28. Santhanagopalan, S.; Ramadass, P.; Zhang, J. Z. *J. Power Sources* **2009**, *194*, 550.
29. Xu, J.; Lan, C.; Qiao, Y.; Ma, Y. *Appl. Therm. Eng.* **2017**, *110*, 883.
30. Lan, C.; Xu, J.; Qiao, Y.; Ma, Y. *Appl. Therm. Eng.* **2016**, *101*, 284.
31. MikolajczakKahn, C.; White, M. K.; Long, R. T. Lithium-Ion Batteries Hazard and Use Assessment; Springer Science & Business Media, Berlin, **2012**.
32. Gray, A. P. *Thermochim. Acta* **1970**, *1*, 563.
33. Sahagian, K.; Bair, H. Transition Temperature Microscopy: Interpreting the Morphology of an Immiscible Polymer Blend, Anasys Instrument, California, **2012**.
34. Miyazaki, T.; Takeda, Y.; Akasaka, M.; Sakai, M.; Hoshiko, A. *Macromolecules* **2008**, *41*, 2749.
35. He, L.; Xu, Q.; Hua, C.; Song, R. *Polym. Compos.* **2010**, *31*, 921.